ARTICLES
https://doi.org/10.1038/s41551-019-0372-9

nature biomedical engineering

There are amendments to this paper

Rapid volumetric optoacoustic imaging of neural dynamics across the mouse brain

Sven Gottschalk[1], Oleksiy Degtyaruk[1], Benedict Mc Larney[1,2], Johannes Rebling[1,2,3,4,5,6], Magdalena Anastasia Hutter[1,7], Xosé Luís Deán-Ben[1,3,4,5,6], Shy Shoham[8,9,10]* and Daniel Razansky[1,2,3,4,5,6]*

Efforts to scale neuroimaging towards the direct visualization of mammalian brain-wide neuronal activity have faced major challenges. Although high-resolution optical imaging of the whole brain in small animals has been achieved ex vivo, the real-time and direct monitoring of large-scale neuronal activity remains difficult, owing to the performance gap between localized, largely invasive, optical microscopy of rapid, cellular-resolved neuronal activity and whole-brain macroscopy of slow haemodynamics and metabolism. Here, we demonstrate both ex vivo and non-invasive in vivo functional optoacoustic (OA) neuroimaging of mice expressing the genetically encoded calcium indicator GCaMP6f. The approach offers rapid, high-resolution three-dimensional snapshots of whole-brain neuronal activity maps using single OA excitations, and of stimulus-evoked slow haemodynamics and fast calcium activity in the presence of strong haemoglobin background absorption. By providing direct neuroimaging at depths and spatiotemporal resolutions superior to optical fluorescence imaging, functional OA neuroimaging bridges the gap between functional microscopy and whole-brain macroscopy.

Mammalian brain function arises through multiscale interactions in a highly interconnected, complex network of cortical and subcortical neurons[1]. Its understanding relies heavily on experimental methods for monitoring neuronal activity at different spatial and temporal scales[2]. Whole-brain activity is typically imaged in both humans and small animals using methods that only indirectly reflect neuronal activity[3–5]; thus, recent efforts towards directly mapping neural network function have focused on fluorescence microscopy and the emerging toolbox of calcium and voltage indicators[6]. Techniques such as two-photon microscopy can visualize the activity of thousands of neurons across multiple cortical layers[7]. However, optical brain microscopy approaches generally require invasive methods (namely, skull and/or scalp removal) and are further unable to resolve large-scale neuronal activity across entire rodent brains due to intense photon scattering. Despite recent developments in fluorescence microscopy[8–10], achieving imaging rates exceeding 1 $mm^3 s^{-1}$ is still challenging[2,10] and real-time, direct monitoring of large-scale neuronal activity in the mouse brain remains an unmet need.

Hybrid optoacoustic (OA) imaging techniques are ideally suited for real-time volumetric brain interrogations due to their intrinsic resilience to light scattering with a single laser pulse sufficient for inducing OA responses in the entire imaged tissue volume[11]. This provides an optimal trade-off between volumetric imaging rates and spatial resolution not achievable with other neuroimaging modalities[11–13]. Broadband ultrasound waves are generated by transient light absorption, enabling high-resolution imaging of optical contrast at centimetre-scale depths in tissue[14,15]—an order of magnitude gain over state-of-the-art optical microscopy. In addition, haemoglobin manifests excellent endogenous absorption contrast, and OA naturally attains label-free high-fidelity images of vascular anatomy, blood oxygenation level and their respective dynamics, enabling the assessment and monitoring of multiple activity-related haemodynamic parameters in health and disease[12,13,15–20].

Can the benefits of OA imaging be harnessed towards direct neuronal activity imaging? In recent work, we demonstrated robust calcium-dependent OA contrast using a genetically encoded calcium indicator (GECI) in zebrafish larvae and excised brains[11]. While promising, the initial proof-of-concept demonstrations left important questions unanswered, ranging from the basic ability to image calcium responses in large and highly scattering and absorbing mammalian brains to whether the method is sensitive enough to observe natural sensory responses relative to the high background haemoglobin absorption signals at GCaMP excitation wavelengths. Here, we devised customized functional OA neuro-tomography setups to demonstrate and characterize the capacity for real-time volumetric imaging of calcium transients across mouse brains expressing GECIs, further demonstrating that the OA method is sufficiently sensitive in detecting distributed sensory responses and setting the stage for future advances.

Results

Preparation of an isolated brain. To study the fundamental ability to optoacoustically image whole-brain calcium dynamics in the mammalian brain, we first developed and validated an isolated brain preparation from GCaMP6f-expressing mice (see Methods for details of the model) and a custom imaging setup continuously perfused with artificial cerebrospinal fluid (ACSF). The blood-free

[1]Institute for Biological and Medical Imaging, Helmholtz Center Munich, Neuherberg, Germany. [2]Faculty of Medicine, Technical University of Munich, Munich, Germany. [3]Faculty of Medicine, University of Zurich, Zurich, Switzerland. [4]Institute of Pharmacology and Toxicology, University of Zurich, Zurich, Switzerland. [5]Institute for Biomedical Engineering, ETH Zurich, Zurich, Switzerland. [6]Department of Information Technology and Electrical Engineering, ETH Zurich, Zurich, Switzerland. [7]Department of Electrical and Computer Engineering, Technical University of Munich, Munich, Germany. [8]Tech4Health Institute, New York University Langone Health, New York, NY, USA. [9]Neuroscience Institute, New York University Langone Health, New York, NY, USA. [10]Department of Ophthalmology, New York University Langone Health, New York, NY, USA. *e-mail: shoham@nyu.edu; daniel.razansky@uzh.ch

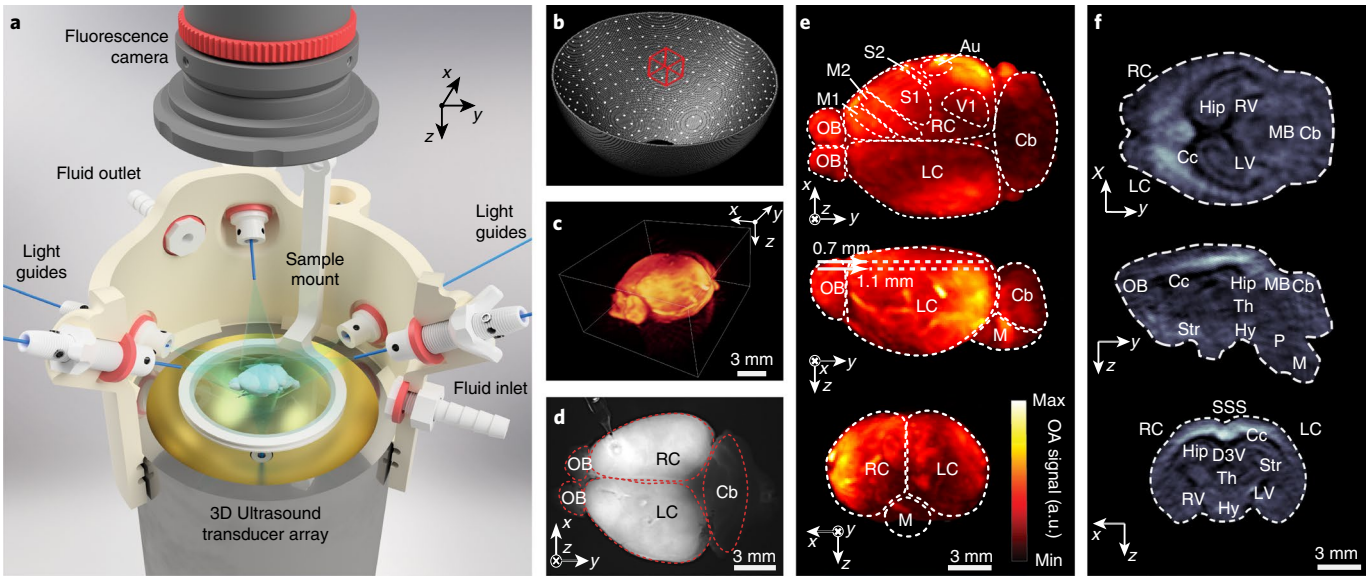

Fig. 1 | Bi-modal OA and fluorescence imaging of isolated brains. a, 3D rendering of the imaging setup featuring a 512-element spherical matrix transducer array inserted into a custom-made 3D-printed holder. The holder features an inlet and outlet to facilitate perfusion with ACSF while the excised brain is placed on top of a transparent polyethylene foil that is attached to the submerged sample mount. The brain is evenly illuminated via seven light guides (fibres) and a sensitive scientific complementary metal-oxide semiconductor camera is positioned at the top for concurrent wide-field fluorescence imaging. **b**, Distribution of detection elements on the spherical array, with its effective volumetric imaging FOV indicated by the red bounding box. **c**, Representative volumetric OA data recorded from an excised GCaMP6f-expressing brain at an excitation wavelength of 488 nm. **d**, Corresponding planar fluorescence image. The glass capillary visible on top of the right cortex (RC) was used for intracortical injections. **e**, Maximum intensity projections (axial, top; sagittal, middle; and coronal, bottom) of the 3D OA dataset shown in **c**. **f**, Representative coronal (top), sagittal (middle) and transverse orthoslices (bottom) of the 3D OA image acquired at 590 nm. In **c**–**f**, $n = 4$ independent experiments. Au, auditory cortex; Cb, cerebellum; Cc, corpus callosum; D3V, dorsal third ventricle; Hip, hippocampus; Hy, hypothalamus; LC, left cortex; LV, left ventricle; M, medulla; M1, primary motor cortex; M2, secondary motor cortex; MB, midbrain; OB, olfactory bulb; P, pons; RV, right ventricle; S1, primary somatosensory cortex; S2, secondary somatosensory cortex; Str, striatum; Th, thalamus; V1, primary visual cortex.

model eliminates background haemodynamic signals, thus allowing for an unequivocal initial characterization of the calcium-related OA signal variations. It further enables deeper penetration of the 488 nm light used for the GCaMP excitation. The isolated brain model exhibits high viability and functional neuronal activity for several hours (Supplementary Figs. 1–3) and realistic optical light-scattering and indicator responses. To evaluate neuronal viability of the in vitro model, we intracortically injected isolated brains of CD-1 mice ($n = 3$) with 10 kD dextran-conjugated Texas Red, an anterograde/retrograde tracer transported by live neurons[21]. The tracer stained structures up to 2 mm away from the injection site, with distant staining observed exclusively in the viable dextran-conjugated dye group (Supplementary Fig. 1c–e). We further recorded electroencephalography (EEG) signals from the cortices of isolated brains perfused in oxygenated ACSF ($n = 3$) versus non-vital controls ($n = 3$) and in vivo recordings ($n = 3$) to evaluate the preparation's electrophysiological function. We observed that injection of the epileptic drug pentylenetetrazol (PTZ) caused significant signal amplitude increases in EEG recordings, particularly in the higher 10–20 Hz frequency range in both isolated and in vivo brains, but not in the non-vital control brains (Supplementary Fig. 3a), nor following injection of a tenfold lower PTZ concentration[22] (Supplementary Fig. 3b).

Volumetric OA and planar fluorescence of calcium activity in whole isolated mouse brains. The developed hybrid imaging system allows for volumetric OA monitoring of resting and stimulus-evoked calcium dynamics concurrently with planar fluorescence imaging (Fig. 1). In the experimental setup, seven optical fibres coupled to a pulsed laser source equally illuminated the brain from multiple directions while planar fluorescence and volumetric OA images were simultaneously captured using a sensitive camera and hemispherical-matrix ultrasound detection array (see schematic in Fig. 1a and Methods for details). The 512-element spherical matrix transducer array with 5 MHz central frequency and 140° angular tomographic coverage (Fig. 1b) was specifically designed to provide a field of view (FOV) of ~2 cm^3, effectively covering the entire mouse brain with nearly isotropic three-dimensional (3D) resolution of ~150 µm (see characterization data in Supplementary Fig. 4a–c). This corresponds to about one million individual voxels that can be visualized within the FOV at a volumetric imaging rate of 100 Hz (the maximum pulse repetition rate of the excitation laser). The system affords the acquisition of volumetric OA images covering the entire GCaMP6f-expressing brain along the transverse, sagittal and coronal planes with high resolution (Fig. 1c,e; $n = 4$ brains imaged), providing stark qualitative improvement over diffuse, surface-weighted two-dimensional wide-field fluorescence image lacking depth resolution (Fig. 1d). A range of gross anatomical features can be identified in the excised brains, such as the cortices, cerebellum, medulla, thalamus and hippocampus (Fig. 1e,f), demonstrating the system's ability to volumetrically capture information from the entire brain.

OA measurements of purified GCaMP6f proteins (Fig. 2a) rendered spectrally specific calcium-dependent absorption changes, suggesting that calcium concentration changes should be optoacoustically detectable in addition to their fluorescence signature. We therefore used the new system to acquire activity videos in isolated GCaMP6f mouse brains resulting from frontal-cortical injection of PTZ ($n = 4$). This neuro-activating agent is assumed to interfere with GABAergic signalling and actuates fast seizure-like activity in the nervous system[23]. Large OA responses of up to 150% were readily observed following the injection (Fig. 2b), appearing to spatially

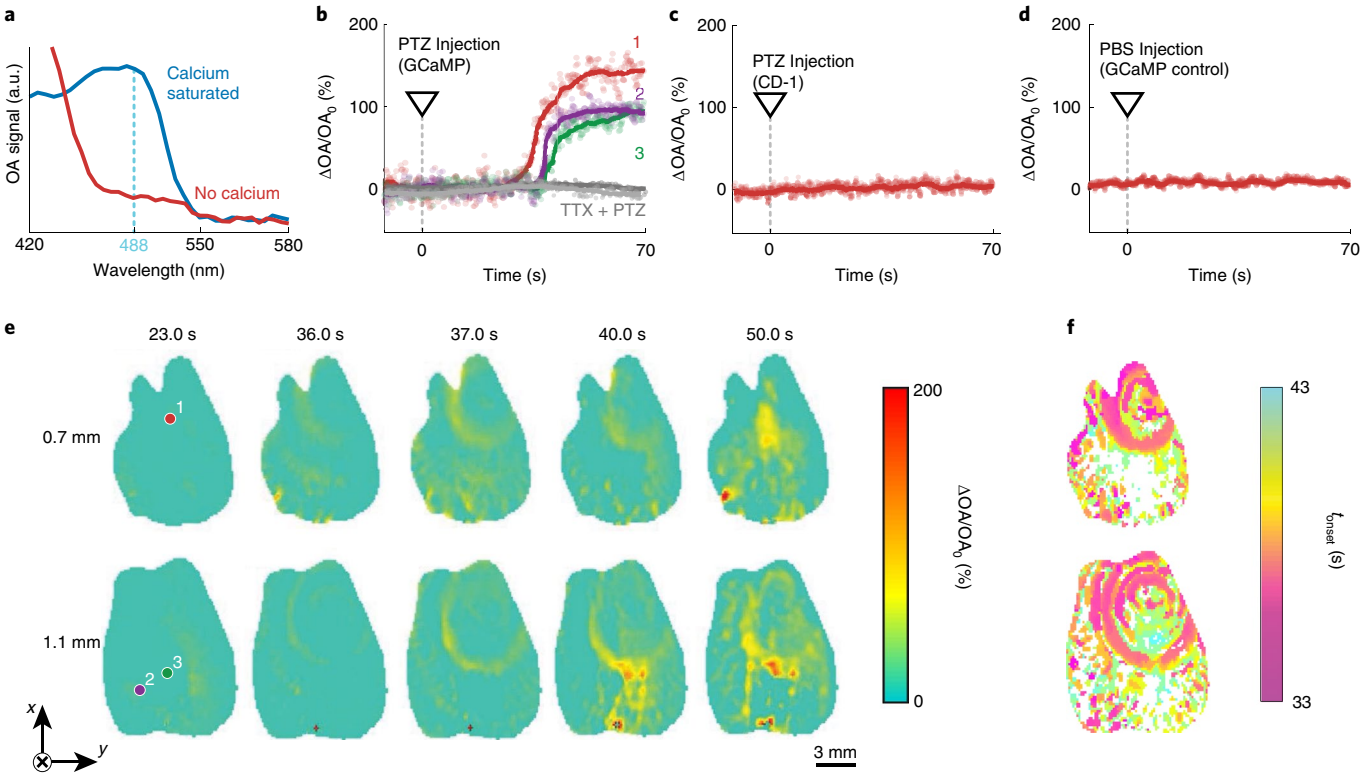

Fig. 2 | Whole-brain volumetric OA imaging of neuronal activation in the isolated brain model. a, Optoacoustically measured absorption spectrum of purified calcium-saturated (blue) and calcium-free (red) GCaMP6f proteins. The dotted line indicates the maximum difference in OA signal at 488 nm between the two protein states ($n = 2$ independent experiments). **b**, Time traces of the normalized OA data, along with the moving averages over 50 image frames (solid lines 1, 2 and 3), are shown from individual voxels whose positions are indicated in **e**. Notably, the activation first occurs in the red voxel located close to the injection site (see the glass capillary location in Fig. 1d), slowly propagating into the rest of the brain (purple and green voxels). Grey traces represent TTX injected 180 s before PTZ, abolishing the activation ($n = 4$ independent experiments for PTZ injection and $n = 3$ for TTX + PTZ). **c**, OA recordings from a control experiment with an isolated CD-1 mouse brain not expressing GCaMP6f proteins. No changes due to PTZ injection are detected ($n = 3$ independent experiments). **d**, Results of an additional control experiment in which an isolated GCaMP6f-expressing brain was injected with PBS, resulting in no OA signal changes ($n = 3$ independent experiments). **e**, Temporal evolution of the relative OA signal changes ($\Delta OA/OA_0$) in two representative slices located at depths of 0.7 mm and 1.1 mm in a GCaMP6f-expressing brain (the slice locations are indicated in Fig. 1e). Injection of the PTZ neurostimulant was done at $t = 0$ s. The indicated voxels 1, 2 and 3 correspond to the solid lines in **b** ($n = 4$ independent experiments). **f**, Onset activation map for the experiment shown in **a**, generated for each image voxel by calculating the time point (t_{onset}) when the relative OA signal change ($\Delta OA/OA_0$) exceeded three times the standard deviation of the background signal (before the PTZ injection). The white colour represents inactivated voxels ($n = 4$ independent experiments).

propagate around the injection site (see the location of the glass capillary in Fig. 1d) and into the uninjected hemisphere (Fig. 2e,f). This is consistent with previous observations of PTZ-induced brain-wide propagating calcium waves[24], putatively indicating the preservation of inter-hemispheric communication in this in vitro model. Similar changes were also observed in the simultaneously acquired wide-field planar fluorescence images (Supplementary Fig. 5a,c), independently validating that the detected OA signals directly correspond to neuronal calcium dynamics. These responses were abolished during concurrent injections of the sodium channel blocker tetrodotoxin (TTX), a potent suppressor of neuronal activity[25] (Fig. 2b). PTZ injection into control CD-1 mouse brains that did not express GCaMP6f resulted in no detectable OA or fluorescence signal increases ($n = 3$; Fig. 2c and Supplementary Fig. 5b,d), as was the case for control phosphate buffered saline (PBS) injections into GCaMP6f-labelled brains ($n = 3$; Fig. 2d and Supplementary Fig. 5e). Notably, the observed relative fluorescence changes were an order of magnitude smaller (only up to 30% above baseline), probably due to the diffuse nature and higher background noise of the wide-field fluorescence modality.

Non-invasive 3D OA imaging of the whole mouse brain in vivo. Next, we explored non-invasive (through intact skin and skull) volumetric in vivo OA recordings from the whole mouse brain using a customized experimental arrangement. Here, the ultrasound array's orientation was reversed and fluorescence versus OA imaging was performed sequentially due to geometric constraints of the in vivo measurement setup (Fig. 3a and Supplementary Fig. 6). GCaMP6f expression was clearly visible in the somatosensory cortex of the transgenic mice in vivo (Fig. 3b). The 3D OA images mainly exhibit vascular contrast related to the strong light absorption by haemoglobin (Fig. 3c). In addition, the limited light penetration at the peak excitation wavelength of GCaMP6f (488 nm) is evident: at 488 nm, clear contrast is preserved up to ~1.5 mm in depth (Fig. 3c), while images at the 650 nm wavelength (where blood absorption diminishes significantly) clearly show visible absorption contrast across the entire brain down to ~7 mm depth (Fig. 3d). The fluorescence signal photo-bleaches at a moderate rate of ~5% signal loss per 100 s of imaging (Fig. 3e, left) under experimental illumination conditions (~3 mJ cm^{-2} excitation light fluence reaching the scalp surface). This rate is consistent with the bleaching rate of the OA signal

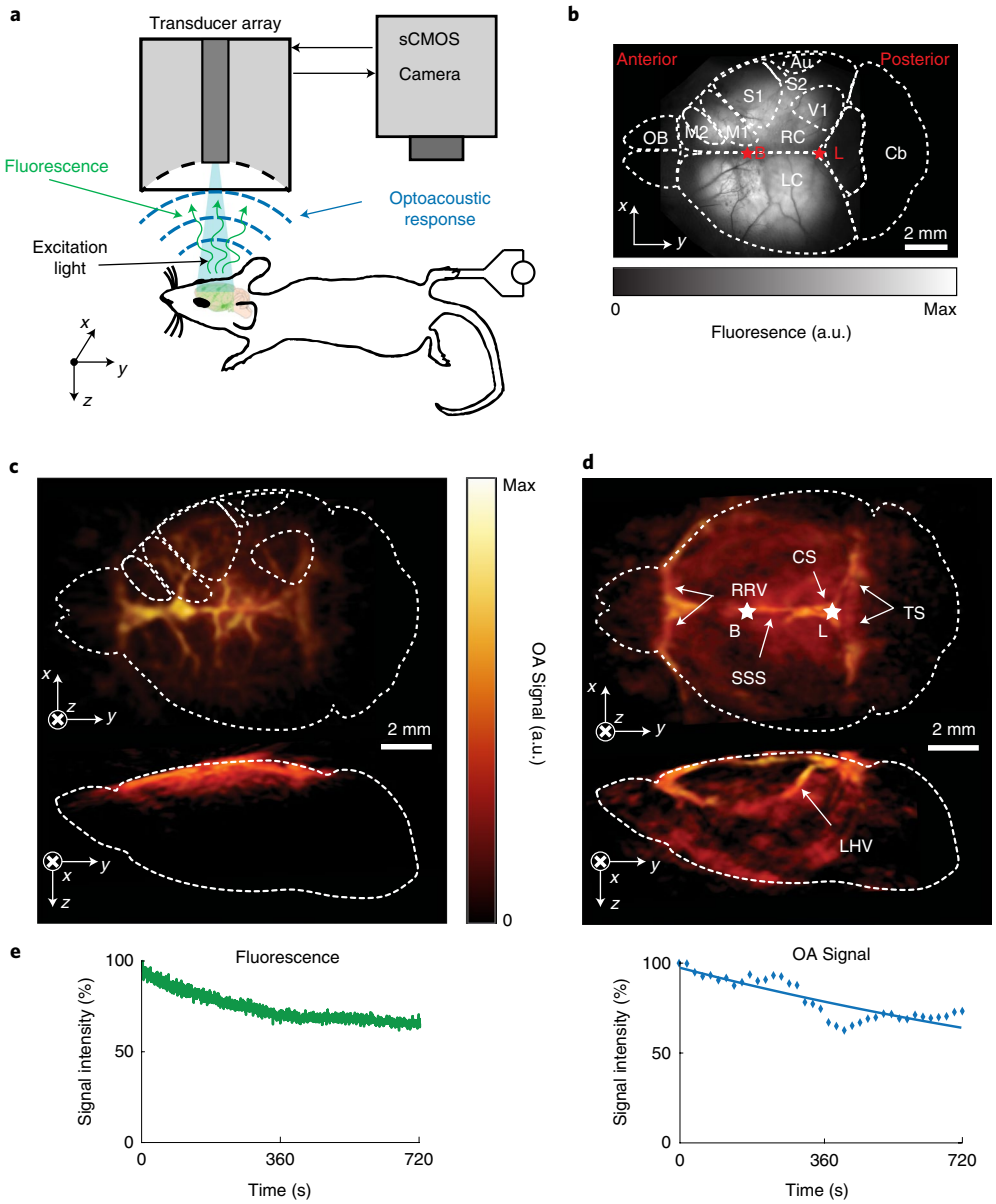

Fig. 3 | Non-invasive imaging of the GCaMP6f brain in vivo. a, Experimental schematic of the hind paw electrical stimulation experiment with alternate imaging in either OA or fluorescence mode. sCMOS, scientific complementary metal-oxide semiconductor. **b**, Representative planar fluorescence image of a GCaMP6f mouse brain. The approximate bregma and lambda skull landmarks (red stars labelled B and L, respectively) are also indicated ($n=3$ biologically independent animals). **c**, Maximum intensity projections of the representative volumetric OA image recorded non-invasively from a GCaMP6f-expressing mouse brain at 488 nm. Note the shallow penetration depth of 1–2 mm at this wavelength ($n=3$ biologically independent animals). **d**, Maximum intensity projections of the volumetric OA images recorded non-invasively at 650 nm in vivo, showing the whole-brain recording capacity of the system down to a depth of ~7 mm. Bregma and lambda skull landmarks are indicated by white stars and labelled B and L, respectively. Major veins are visible and have been labelled accordingly. $n=3$ biologically independent animals. CS, confluence of sinuses; LHV, longitudinal hippocampal vein; RRV, rostral rhinal vein; TS, transverse sinus. **e**, The GCaMP6f protein is prone to bleaching over the course of the imaging experiment. Left, normalized average fluorescence signal of the whole-brain area. Right, average OA signal decay of each stimulus cycle (blue diamonds), with the linear fit shown by a solid blue line ($n=3$ biologically independent animals).

(Fig. 3e, right) and with earlier observations[26]. The fluorescence also recovered to pre-imaging levels within 24 h due to protein recycling (data not shown). To further minimize protein bleaching, the laser beam could potentially be blocked for time intervals when no activity is expected.

Brain-wide OA imaging of stimulus-locked calcium responses in vivo. The in vivo imaging setup was then used to explore volumetric recordings of somatosensory-evoked rapid calcium transients in GCaMP6f/6s-expressing mice. To detect stimulus-locked fluorescence and OA calcium signals (Fig. 4a,b) while minimizing background haemodynamic responses[27], brief 50 ms electrical stimulation pulses were repeatedly delivered to the hind paw every 20 s (Fig. 4c). The time-lapse OA imaging recordings were carried out at 25 Hz, and fluorescence images were acquired at a lower rate of 6.25 Hz. Clearly resolvable stimulus-locked OA responses to each stimulus were readily observed in GCaMP6f mice ($n=4$ experiments in 3 mice), with typical average traces reaching a peak at ~360 ms

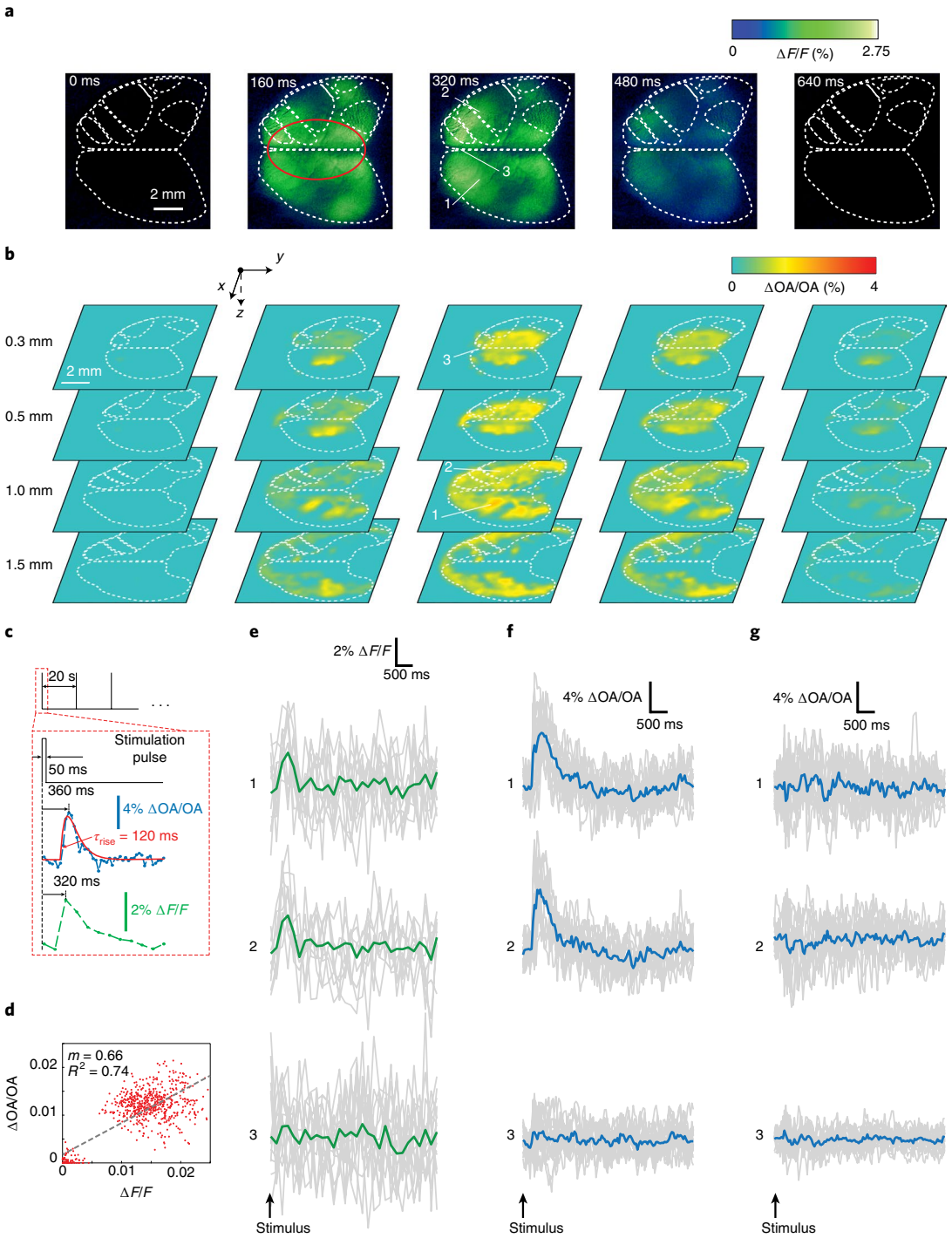

Fig. 4 | Non-invasive imaging of somatosensory-evoked rapid calcium transients in the GCaMP6f brain in vivo. a, Temporal sequence of fluorescence-recorded brain activation maps ($\Delta F/F$) in response to the current stimulus at $t = 0$ at the right hind paw. Functional regions of the brain are indicated as dashed white lines. **b**, Four-dimensional optoacoustically recorded brain activation maps ($\Delta OA/OA$) in response to the stimulus at $t = 0$. Slices across the entire brain are shown located at different depths from the brain surface. Functional regions of the brain are indicated as dashed white lines. **c**, Schematic of the electrical paw stimulation paradigm. Top, a 50-ms-long stimulus was repeated every 20 s. Bottom, representative single-voxel OA and single-pixel fluorescence time traces. Note that the volumetric OA recordings (blue) were carried out at a rate of 25 Hz, versus 6.25 Hz for planar fluorescence (green). τ_{rise} is defined as the time required for the OA signal to rise from 20–80% of its maximum. **d**, Relative OA signal increase versus relative fluorescence signal increase for a set of points in the region indicated by a red oval in **a** and for three different time points (160, 320 and 640 ms). The maximum of all slices is taken for calculating the relative OA signal increase. The dashed line of the best fit was determined using a least-squares method; its slope and coefficient of determination are denoted by m and R^2, respectively. **e**, Background-subtracted and normalized ($\Delta F/F$) fluorescence signal traces following the stimulus in three pixels located in S1 on each hemisphere (1 and 2) and inside the SSS (3). **f**, Background-subtracted and normalized ($\Delta OA/OA$) OA signal response traces for single voxels located bilaterally in S1 outside major vessels (voxels 1 and 2; approximately 1 mm depth) and inside the SSS (voxel 3). **g**, Background-subtracted and normalized ($\Delta OA/OA$) OA signal traces following the stimulus in control wild-type mice for single voxels at similar locations as in **f**. $n = 4$ independent experiments and $n = 3$ biologically independent animals for all panels.

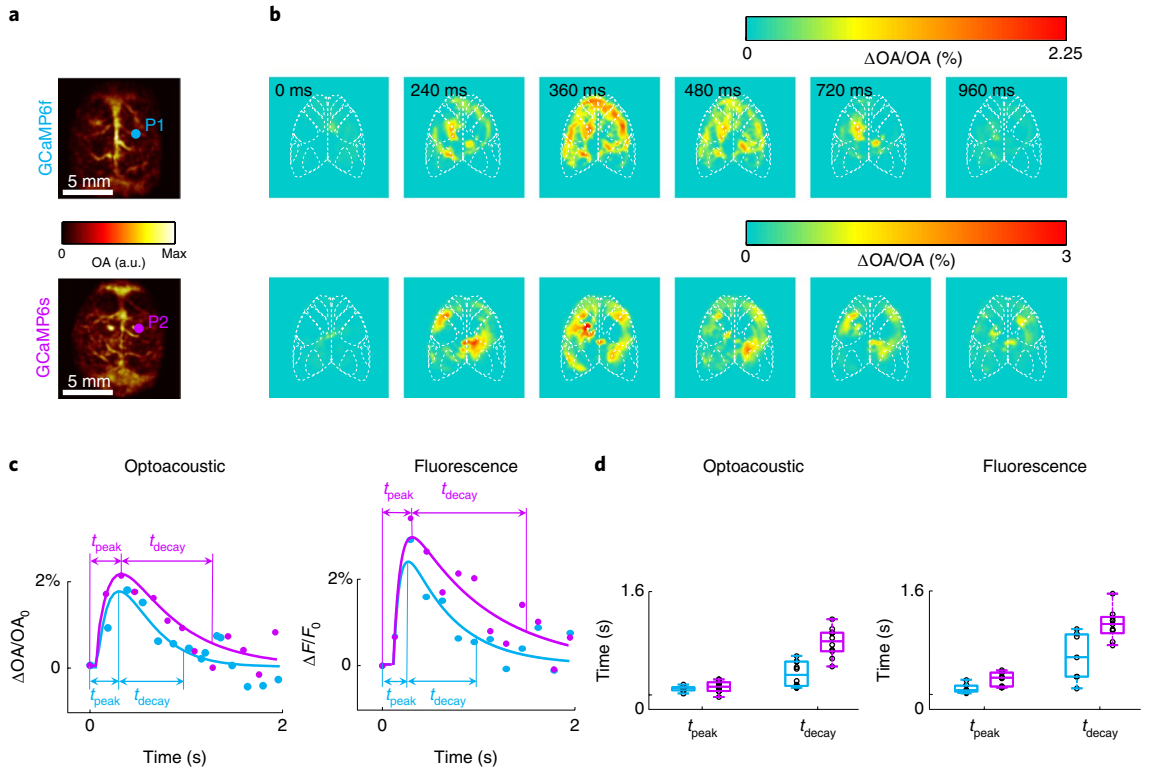

Fig. 5 | Comparison of GCaMP6f and GCaMP6s responses to electrical stimulation of the right or left hind paw. a, Maximum intensity projection along the depth direction of the 3D images of GCaMP6f- (top) and GCaMP6s-expressing (bottom) mice. P1 and P2 indicate the locations for the time profiles shown in **c**. **b**, Relative increase in OA signal with respect to the baseline for a slice at approximately 1 mm depth at different time points following the stimulation pulse for GCaMP6f- (top) and GCaMP6s-expressing (bottom) mice. The baseline is defined as the average of 250 frames from 10–20 s after the stimulations pulse. **c**, Fitted time profiles of the relative increase in OA (left) and fluorescence signals (right) corresponding to the P1 and P2 positions in **a** for the GCaMP6f (blue) and GCaMP6s mice (violet). **d**, Box plots of the statistical distribution of the estimated signal time-to-peak (t_{peak}) and decay (t_{decay}) values within the cortex. Data points (ten independent pixels/voxels for each box plot) are also shown as black circles. The maximum, minimum, median, and 25th and 75th percentiles (in s) for each plot are, respectively, 0.3198, 0.2001, 0.2806, 0.2413 and 0.2806 for $t_{peak,OA,6f}$; 0.4202, 0.1609, 0.3002, 0.2413 and 0.3610 for $t_{peak,OA,6s}$; 0.7083, 0.2766, 0.4513, 0.3021 and 0.6318 for $t_{decay,OA,6f}$; 1.2145, 0.5749, 0.9153, 0.7809 and 1.0320 for $t_{decay,OA,6s}$; 0.3993, 0.2205, 0.2566, 0.2395 and 0.3183 for $t_{peak,F,6f}$; 1.0010, 0.2912, 0.4295, 0.3114 and 0.5005 for $t_{peak,F,6s}$; 1.0841, 0.2830, 0.7029, 0.4412 and 1.0118 for $t_{decay,F,6f}$; and 2.8850, 0.8673, 1.1777, 1.0681 and 1.2842 for $t_{decay,F,6s}$. $n = 2$ independent animal experiments for the right and left hind paw, respectively.

post-stimulation, then rapidly decaying and reaching the baseline level at ~0.8 s post-stimulation (Fig. 4b,c), paralleling the temporal patterns of the observed fluorescence responses. Interestingly, the normalized OA signal transients (ΔOA/OA) in the activated brain area were spatially correlated with, and generally stronger than, the separately measured normalized $\Delta F/F$ fluorescence responses (Fig. 4d), despite the very high blood background absorption levels inherently reflected in the OA signals. This difference is presumably attributable to intrinsic differences between these modalities, where the fluorescence signal traces effectively average calcium responses from a larger volume. Such differences can be particularly prominent at deep locations, as also observed in the isolated brain experiments where OA and fluorescence responses were measured concurrently. Additionally, the in vivo OA recordings from deeper slices (Fig. 4b) exhibit distinct activation patterns not resolvable in the surface-weighted mesoscopic fluorescence images affected by the strong light scattering in the scalp, skull and brain. Thus, OA imaging provides additional depth information without sacrificing speed, allowing 3D resolution of neuronal activity with unparalleled spatiotemporal resolution (Supplementary Fig. 4d–f). Note that signal averaging across repeated responses results in better rejection of noise and clearer distinction of the activation peaks (Fig. 4e,f). No OA signal changes were detected in wild-type mice under the same brief 50 ms electrical stimulation paradigm (Fig. 4g), confirming that this particular paradigm does not induce detectable haemodynamic changes.

We further analysed the functional OA signals of different voxels located in the somatosensory cortex and a major vessel (the superior sagittal sinus (SSS)). Clear bilateral activations can be seen in both planar fluorescence (Fig. 4e) and OA traces recorded from the somatosensory cortical areas outside major vessels at approximately 1 mm depths (Fig. 4f), and also in the stimulus-locked four-dimensional spatiotemporal OA image sequences (Fig. 4b), which is consistent with previous reports of bilateral somatosensory cortical activations[28,29]. Bilateral activations were also consistently observed in control experiments using different strengths of the stimulation pulse, a different breathing gas, and after using analgesia before the stimulation experiments (Supplementary Fig. 7). To further corroborate that the detected signals correspond to calcium transients rather than haemodynamic changes, we imaged GCaMP-negative (wild-type) mice as controls using the same stimulation paradigm, observing no signal spikes (Fig. 4g). In contrast, when changing the stimulation paradigm to a longer stimulation pulse train known to induce robust bilateral haemodynamic responses in blood-oxygen-level-dependent functional MRI[30], OA signal changes could be clearly observed using multispectral measurements (Supplementary Fig. 8). These findings show that both fast calcium-related activity and slow haemodynamic responses can be effectively measured optoacoustically.

We also compared the OA responses of mice expressing fast GCaMP6f and slow GCaMP6s protein variants (Fig. 5a) and subjected both to the same hind paw stimulation paradigm. Similar brain activation patterns and relative OA signal increases were observed for both mouse strains (cortical layers at ~1 mm depth shown in Fig. 5b). The peak responses for GCaMP6f and GCaMP6s signals were produced at approximately the same time point following the stimulation pulse, while a slower decay was clearly observed in the GCaMP6s signals (left panels in Fig. 5c,d). These observations are consistent with the time constants in fluorescence measurements (right panels in Fig. 5c,d; images not shown) and previously reported protein dynamics[31].

Discussion

Extensive efforts in optical neuroimaging are directed towards increasing the effective FOV and volumetric imaging rates of functional microscopy techniques, but the inherent advantages of OA approaches may allow the mapping of brain activity at depths and spatiotemporal scales not achievable by other modalities. Our study examines fast OA signatures of GECIs in the densely vascularized and light-scattering mammalian brain, further showing that changes in their fluorescence are directly related to the OA responses, both in vitro and in vivo. We found that despite strong background haemoglobin absorption at the effective imaging wavelengths of GCaMP-type calcium indicators, the OA modality is sensitive enough to record sensory-evoked brain activity via GCaMP6f and GCaMP6s calcium-related signal changes that were in fact stronger than the corresponding fluorescence responses. This represents an important milestone for direct OA neuroimaging, which is further empowered by its deep tissue real-time 3D imaging performance and the capacity to sense multiple cerebral oxygenation and haemodynamic parameters deep in the living rodent brain[11,17], thus enabling direct investigations into mechanisms of neurovascular coupling[32].

Calcium transients and haemodynamic responses occur at significantly different time scales; hence, they can be distinguished using high-resolution temporal, as well as auxiliary multispectral, OA information (Supplementary Fig. 8). Moreover, the capacity to potentially distinguish brain-wide time profiles associated with specific GECIs further empowers OA with unique capabilities for assessing normal and dysregulated neural network interactions, as well as for investigating the roles of other central nervous system cell types. Future work therefore includes implementation of the common neural network analysis strategies employed in mesoscopic fluorescence imaging and other functional neuroimaging techniques, such as resting-state networks, dynamic causal modelling and stimulus encoding–decoding analyses[33].

The imaging system was designed to capture neuronal dynamics in real time as true 3D information across effective FOVs of ~2 cm^3, covering an entire mouse brain at a spatial resolution of 150 µm. In contrast, imaging a whole rodent brain with an advanced optical microscopy technique such as OCT still requires slicing it to ~200-µm-thick layers[34]. To demonstrate this capability, we first tracked whole-brain calcium dynamics in a blood-free isolated brain preparation. The isolated whole brain has clear advantages for studying large-scale recording capacity over conventional in vitro preparations such as neuronal cultures[2] or brain slices[35], realistically capturing both long-range and whole-brain neural network interactions and overcoming the brain's light-scattering properties. Multiple aspects of our method can be further improved. Imaging scalability can readily be achieved using high-frequency matrix array probes for better spatial resolution, but at the expense of a smaller FOV[11], and of increased skull-mediated distortions of the high-frequency ultrasound wave components[36]. In the current implementation, the mouse's head is fixed during the acquisition to prevent motion. Ultrasound arrays with a relatively low number of elements attached to a rodent's head, to acquire ultrasound echoes and OA signals[13,37], have recently been designed. Thus, our proposed technique can potentially be adapted to study freely behaving animals. GCaMP6f, the fastest GCaMP6 family indicator[31], was chosen here since the system's rapid acquisition time (10 ms) dictated that the indicator dynamics limit the effective temporal resolution. Slower indicator variants can be imaged instead for improved signal characteristics, while other major advances can arise from the development and use of new activity indicators by leveraging the wide tunability of the lasers used in our technology. Other options include the newer generations of GCaMP-type[38,39] and red-shifted probes such as RGECO[40], although their peak extinction still falls within the range of strong absorption by haemoglobin. The long-anticipated development of far-red and near-infrared calcium indicators[41] with absorption peaks above 650 nm may eventually enable OA imaging in the presence of a significantly lower blood absorption background, reaching deeper brain regions in vivo, thus potentially enabling non-invasive monitoring of activity across the entire living rodent brain (Fig. 3d).

Methods

Isolated brain preparation. The brains of female CD-1 and GCaMP6f-expressing mice aged 8–12 weeks were used. This animal experiment was carried out in full compliance with the institutional guidelines of the Institute for Biological and Medical Imaging, along with approval from the Government District of Upper Bavaria. Mice were injected intraperitoneally with a lethal dose of ketamine/xylazine. Subsequently, intracardiac perfusion with ice-cold PBS was performed to remove blood from the brain. For this, once the animal was completely anaesthetized, as determined by the absence of a toe-pinch reflex, surgery began with an incision from the mid-abdomen to the sternum. The ventral part of the rib cage was removed to allow access to the heart. Intracardiac perfusion was then carried out after inserting a 25G butterfly needle into the left ventricle of the heart, followed by an incision into the right atrium. The heart was perfused until both the liver and lungs turned white, at which stage decapitation was performed. Next, all tissue and skin surrounding the skull was removed, and the skull was rinsed with ice-cold PBS to remove any remaining debris. A cut was then made between the skull and the first cervical vertebra, exposing the brain stem. Using bone scissors, a second cut was made on both sides of the skull, which extended from the foramen magnum to the external auditory meatus, and then from the molar process up to the lachrymal dorsal aspect of the skull (Supplementary Fig. 1b). Using forceps, the upper skull plate, together with the brain, was separated from the lower skull and placed into a Petri dish filled with ice-cold, oxygenated ACSF. The brain was then carefully separated from the skull using forceps, and placed in a second Petri dish filled with fresh ACSF. Any remaining hair, debris and blood vessels were removed using fine forceps and a pipette.

Dextran tracing. Axonal tracer transport requires intact, functioning neurons, and dextran-amines coupled to fluorescent molecules are known for being transported in both the anterograde and retrograde direction[21]. 0.5 µL of 10 kDa dextran coupled to Texas Red (Thermo Fisher Scientific) was injected directly into the cortex of the excised brain preparations to validate the functionality of axonal transport. The experimental setup is illustrated in Supplementary Fig. 2a. Freshly excised brains were placed in a custom-made chamber filled with ACSF and with a constant supply of carbogen (95% O_2 and 5% CO_2), to keep the solution oxygenized and the pH stable at physiological conditions. For intra-brain injection at a depth of ~1 mm inside the cortex, a wireless robotic injection system (NeuroStar) using a 15–25-µm-diameter glass microcapillary was utilized. As controls, either PBS or Texas Red (without dextran) were injected under the same conditions. Afterwards, the brains were fixated in paraformaldehyde, either immediately after injection or after being kept in oxygenized ACSF at 4 °C in the dark for 1 h. Fixated brains were then sliced into 50-µm-thick sections to evaluate axonal transport. For this, the brains were first dehydrated in a solution of 30% sucrose at 4 °C for 48 h to remove water and prevent ice-crystal formation during cryo-slicing. Subsequently, the brains were embedded in optimum cutting temperature compound (Tissue-Tek O.C.T. compound; VWR) and sliced into 50-µm-thick sections along the coronal plane using a CM1950 cryo-slicer (Leica Biosystems). These cryo-sections were mounted onto microscope slides and air-dried for 20 min in the dark. A coverslip was placed on top of the slices and sealed with Vectashield containing 4′,6-diamidino-2-phenylindole (DAPI) (Vector Laboratories). DAPI stains the DNA and RNA of cells, hence outlining cellular anatomy. Compound brain slice images were captured using an Imager.M2 microscope fitted with shift-free DAPI and Texas Red filter sets (Carl Zeiss). Image acquisition was done using ZEN 2 microscope software (Carl Zeiss).

EEG recording. The experimental setup for EEG recordings from the isolated brains is depicted in Supplementary Fig. 2b. The excised brains were placed in

the custom-made chamber filled with oxygenized ACSF at room temperature. To induce neuronal activity, 5 µl of PTZ (100 mg ml^{-1} in PBS) was directly injected into the cortex using a glass capillary and a robotic injection system (NeuroStar). EEG signals were recorded via two custom-made needle electrodes connected to a DP-311 differential amplifier (Warner Instruments). The amplified signals were digitized by means of a PowerLab 26T data acquisition module (ADInstruments) controlled through a host PC running the LabChart 8 software (ADInstruments). The amplifier gain value was set to 100 due to relatively low signal strengths for EEG recordings in isolated brains. For comparison, the in vivo EEG of a CD-1 mouse was also recorded, as described previously[12]. This animal experiment was performed in full compliance with the institutional guidelines of the Institute for Biological and Medical Imaging and with approval from the Government District of Upper Bavaria. To induce widespread brain activity, the epileptic drug PTZ was injected intraperitoneally[24]. For in vivo EEG recording, the amplifier was set to a high pass of 10 Hz, a low pass of 100 Hz and a gain of 100. After baseline recording, 100 µl of PTZ (25 mg ml^{-1} in PBS) was injected intraperitoneally, and EEG signals were recorded for at least 25 min. At the end of the experiment, the mouse was euthanized while still under anaesthesia. The recorded EEG signals were processed using MATLAB (MathWorks) to identify periods of neuronal activity. For this, the spectrograms of the EEG signals were calculated as the short-time Fourier transform with a window of 20 s, which is sufficient to detect higher-frequency components in the range of 10–20 Hz corresponding to seizure-like activity caused by PTZ.

In vivo animal handling. For the in vivo experiments, 8- to 12-week-old female C57BL/6J-Tg(Thy1-GCaMP6f)GP5.5Dkim/J and C57BL/6J-Tg(Thy1-GCaMP6s)GP4.12Dkim/J mice (The Jackson Laboratory; stock numbers 024276 and 025776, respectively), along with 6- to 12-week-old athymic female nude mice (Envigo; stock number *Foxn1*^{nu} 069), were used in full compliance with the institutional guidelines of the Institute for Biological and Medical Imaging and with approval from the Government District of Upper Bavaria. Mice were anaesthetized with isoflurane (2.5% *v/v* for induction) in 100% O_2. When necessary, any fur on the head of the mouse was removed using consumer hair-removal cream before the experiments. To avoid motion artefacts during imaging, the head of the mouse was fixed into a custom-designed stereotactic mouse head holder, which was coupled to an anaesthetic breathing mask (Narishige International). During the experiments, the animals were maintained under isoflurane anaesthesia with 1.0–1.5% *v/v* in 100% O_2 with a flow rate of ~0.7 l min^{-1}, and the physiological parameters (blood oxygenation, heart rate and body temperature) of the animals were continuously monitored using a PhysioSuite physiological monitor (Kent Scientific). The core body temperature was tracked and maintained at ~36 °C using a homeothermic temperature controller coupled to a heating pad, both of which were controlled by the PhysioSuite. For analgesia, a single drop of 125 mg ml^{-1} metamizole was given orally before the experiments (Novalgin; Sanofi-Aventis Deutschland).

Hind paw electrical stimulation. For GCaMP imaging, hind paw stimulation was applied by inserting thin stainless-steel needle electrodes under the skin of the paw in isoflurane-anaesthetized mice. Electrical stimulation with 50 ms pulses at a constant current of 1 mA was employed using a constant current stimulus isolator (Model A365R; World Precision Instruments). The block stimulation paradigm consisted of repeating the pulses every 20 s (Fig. 4c). For the induction and imaging of haemodynamic responses, the following stimulation paradigm was carried out instead: one hundred 500 µs pulses were applied at 0.5 mA every 200 ms for 20 s. Stimulation began 30 s into the imaging cycle to allow baseline activity approximation. The OA or fluorescence data acquisitions were synchronized with the start of the first cycle.

Imaging setup. The OA tomography system used for real-time volumetric acquisition of data consists of a custom-made spherical transducer array (Imasonic SAS). The spherical surface has a 40 mm radius and consists of 512 piezocomposite elements covering an angle of 140° (1.32π solid angle). The elements have a diameter of 2.5 mm, a central frequency of 5 MHz and a 100% detection bandwidth of approximately −6 dB, providing a nearly isotropic resolution of 150 µm around the centre of the spherical geometry and an effective FOV of approximately 2 cm^3. The imaging resolution and FOV were characterized with an agar phantom containing sparsely distributed ~50-µm-diameter polyethylene-absorbing spheres (Cospheric). The image of the phantom (top maximum intensity projection) rendered with the system is displayed in Supplementary Fig. 4. The resolution at the centre of the spherical array was estimated as the mean square difference between the measured sphere's full width at half maximum and its actual diameter. The FOV was estimated as the size of the region containing particles reconstructed with an amplitude higher than 50% of the maximum signal in the images.

Isolated brain imaging. For imaging of the isolated brains, the array was held pointing upwards by a custom-made 3D-printed holder attached to an *x*–*y* positioning platform. The holder further allowed for superfusion of ACSF around the excised brain via an inlet and an outlet, thus establishing a physiological environment supporting brain vitality (Fig. 1a). Excised brains were placed at approximately the centre of the spherical geometry lying on a transparent polyethylene foil with a thickness of ~10 µm. Illumination was provided via a self-made fibre bundle consisting of seven fibres, each with a core diameter of 600 µm. One of the fibres was inserted into a cylindrical cavity of the spherical array to illuminate the bottom part of the brain, while the other 6 fibres were inserted into the holder and equally spaced at 120° in the azimuthal direction, and with polar angles of 5.7 and 37° (Fig. 1a). The illumination source was an optical parametric oscillator-based laser (Innolas) providing short (<10 ns) pulses at a repetition frequency of 100 Hz whose optical wavelength is freely tunable between 420 and 680 nm. The 512 OA signals detected by the matrix array elements were simultaneously digitized with a custom-made data acquisition system (Falkenstein Mikrosysteme) triggered with the Q-switch output of the laser. The digitized signals were transferred to a computer via a 1 Gbit s^{-1} Ethernet connection. To record fluorescence signals, a high-speed scientific complementary metal-oxide semiconductor camera (Andor Technology) was positioned on top of the holder pointing downwards and synchronized with the pulsed laser source. The camera was equipped with a manually focused 105 mm Nikon F mount objective (Nikon) and a 25.4 mm band pass filter (525 nm centre wavelength and 39 nm bandwidth; MF525–39; Thorlabs). The acquisition time of the camera was set to 200 ms, corresponding to the integration of 5 laser pulses.

In vivo imaging experiments. For the in vivo imaging experiments, the OA tomography system was used in a reversed orientation (Supplementary Fig. 6b) The wide-field fluorescence recordings were not performed concurrently due to the lack of access to the imaged area in the in vivo setting. Also, the laser light beam was guided differently from the isolated brain setup (that is, a single custom-made silica fused-end fibre bundle (CeramOptics) was used to broadly illuminate the imaged area from a single direction). At the peak absorption wavelength of calcium-saturated GCaMP6f/6s of 488 nm, the light fluence at the sample was measured to be ~3 mJ cm^{-2} (that is below safe exposure limits for pulsed laser radiation[42]). The same fibre bundle was used to illuminate the shaved mouse head. However, fluorescence imaging was performed separately, with the mouse head illuminated laterally, to avoid blinding the camera, as indicated in Supplementary Fig. 6a.

Imaging of GCaMP responses were done at a 25 Hz laser repetition frequency and a single excitation wavelength of 488 nm. OA imaging of haemodynamic imaging was carried out instead at 20 Hz, with 5 wavelengths (530, 540, 560, 575 and 585 nm). This resulted in an imaging rate of 4 Hz per wavelength and allowed for the unmixing of two blood components: oxygenated haemoglobin and reduced haemoglobin. Total haemoglobin was estimated as the sum of these two components. A 100 µm black microsphere (BKPMS-1.2 90–106 um; Cospheric) was placed in the FOV, immediately above the skin of the mouse, and used to normalize the OA images with the per-pulse laser energy variations (assumed to be proportional to the OA signal of the sphere).

Isolated protein measurements. The OA spectrum of the isolated proteins was measured with the same system by injecting the proteins (~50 µM concentration) in a polyethylene tubing with 0.57 mm inner diameter. The laser was tuned between 420 and 580 nm with 5 nm steps on a per-pulse basis, and averaging of 50 multispectral datasets was performed. For the measurements, the proteins were first diluted in a buffer containing 30 mM 4-morpholinepropanesulfonic acid, 100 mM KCl (pH 7.2) and 1 mM $MgCl_2$ mimicing physiological conditions. Calcium-free and calcium-saturated protein solutions were rendered by subsequently adding 10 mM ethylene glycol-bis(β-aminoethyl ether)-N,N,N′,N′-tetraacetic acid (EGTA) or 100 µM $CaCl_2$, respectively, to the solution.

Imaging data analysis and processing. Volumetric (3D) OA images were reconstructed from the acquired signals using a graphics processing unit-based implementation of a back-projection formula[43]. Before reconstruction, the signals were deconvolved with the impulse response of the transducer array elements, and band-pass filtered with cut-off frequencies of 0.1 and 6 MHz. Reconstruction was performed on a grid of 150 × 150 × 100 voxels^3 (FOV: 15 × 15 × 10 mm^3) to better match the 150 µm spatial resolution of the system. The reconstructed images were normalized with the estimated light fluence distribution $\Phi(\vec{r},t)$ to compensate for light attenuation within the sample according to the light diffusion equation with no transient effects and no internal light sources[44]:

$$\mu_a\Phi(\vec{r},t)-D\nabla^2\Phi(\vec{r},t)=0 \quad (1)$$

where $D=1/3(\mu_a+\mu'_s)$, and μ_a and μ'_s are the optical absorption and reduced scattering coefficient, respectively. The solution of equation (1) for a uniformly illuminated spherical target is given by a modified spherical Bessel function[45] via:

$$\Phi(r,t)=\frac{\Phi_0}{\frac{\sinh(kR)}{kR}}\frac{\sinh(kr)}{kr} \quad (2)$$

where R is the radius of the sphere, r is the distance from its centre, Φ_0 is the fluence at the surface and $k=\sqrt{\mu_a/D}$. A predictive Kalman filter was further applied on a per-slice basis to the time domain of the sequence of reconstructed OA images for noise removal[46].

The effect of bleaching in OA signal decay during the stimulation-evoked activity experiment was estimated as follows. A Kalman filter with a gain of 0.75 was applied to the individual time profiles of the OA signal intensity for a location in the brain having a clear activation peak. The average time profile for all of the cycles was taken as a reference. All profiles were windowed to the initial 4 s following the hind paw stimuli. The OA signal intensity associated with GCaMP as a function of time was estimated by cross-correlation of the individual profiles and the reference profile. A ten-point moving average filter was applied to the calculated cross-correlation values, which were subsequently normalized to the maximum value. An exponential decay function was eventually fitted to these values.

The onset time for the appearance of activity after PTZ injection in the isolated brain experiments was estimated as follows. First, the standard deviation of the background OA signal intensity for each voxel of the reconstructed image was calculated for a window of 300 consecutive frames (40 ms per frame) where no PTZ-related activity occurred. The onset time was estimated by considering the time point at which the OA signal exceeds the standard deviation of the background signal by a factor of 3. It was assumed that no activation was produced at voxels for which the OA signal intensity did not reach this value.

For analysis of the haemodynamics-related OA signal changes, the multispectral OA data were first reconstructed as outlined above on a per-wavelength basis. A spatial moving average of 3 × 3 voxels and a temporal forward-moving average of 10 frames (2.5 s) was applied to the time-lapse volumetric datasets. The images were then unmixed for oxygenated haemoglobin, deoxygenated haemoglobin and total haemoglobin on a per-voxel basis according to their absorption spectrum at the five excitation wavelengths by assuming a linear unmixing model[12,17]. Delta calculations were performed for each component using the first nine frames before stimulation as a baseline estimation. Lastly, a low-pass filter with a cut-off frequency of 0.05 Hz was used to smoothen the resulting temporal profiles.

Reporting Summary. Further information on research design is available in the Nature Research Reporting Summary linked to this article.

Code availability

All custom code generated for this study can be obtained from the corresponding authors on reasonable request.

Data availability

The authors declare that all data supporting the findings of this study are available within the paper and its Supplementary Information. All datasets generated during this study are available from the corresponding authors.

Received: 21 May 2018; Accepted: 19 February 2019;
Published online: 25 March 2019

References

1. Hilgetag, C. C. & Amunts, K. Connectivity and cortical architecture. *eNeuroforum* **7**, 56–63 (2016).
2. Peron, S., Chen, T. W. & Svoboda, K. Comprehensive imaging of cortical networks. *Curr. Opin. Neurobiol.* **32**, 115–123 (2015).
3. Eggebrecht, A. T. et al. Mapping distributed brain function and networks with diffuse optical tomography. *Nat. Photon.* **8**, 448–454 (2014).
4. Errico, C. et al. Transcranial functional ultrasound imaging of the brain using microbubble-enhanced ultrasensitive Doppler. *NeuroImage* **124**, 752–761 (2016).
5. Schulz, K. et al. Simultaneous BOLD fMRI and fiber-optic calcium recording in rat neocortex. *Nat. Methods* **9**, 597–602 (2012).
6. Looger, L. L. & Griesbeck, O. Genetically encoded neural activity indicators. *Curr. Opin. Neurobiol.* **22**, 18–23 (2012).
7. Yang, W. & Yuste, R. In vivo imaging of neural activity. *Nat. Methods* **14**, 349–359 (2017).
8. Bouchard, M. B. et al. Swept confocally-aligned planar excitation (SCAPE) microscopy for high speed volumetric imaging of behaving organisms. *Nat. Photon.* **9**, 113–119 (2015).
9. Dana, H. et al. Thy1-GCaMP6 transgenic mice for neuronal population imaging in vivo. *PLoS ONE* **9**, e108697 (2014).
10. Prevedel, R. et al. Fast volumetric calcium imaging across multiple cortical layers using sculpted light. *Nat. Methods* **13**, 1021–1028 (2016).
11. Dean-Ben, X. L. et al. Functional optoacoustic neuro-tomography for scalable whole-brain monitoring of calcium indicators. *Light Sci. Appl.* **5**, e16201 (2016).
12. Gottschalk, S., Fehm, T. F., Dean-Ben, X. L., Tsytsarev, V. & Razansky, D. Correlation between volumetric oxygenation responses and electrophysiology identifies deep thalamocortical activity during epileptic seizures. *Neurophotonics* **4**, 011007 (2017).
13. Tang, J., Coleman, J. E., Dai, X. & Jiang, H. Wearable 3-D photoacoustic tomography for functional brain imaging in behaving rats. *Sci. Rep.* **6**, 25470 (2016).
14. Dean-Ben, X. L., Gottschalk, S., Sela, G., Shoham, S. & Razansky, D. Functional optoacoustic neuro-tomography of calcium fluxes in adult zebrafish brain in vivo. *Opt. Lett.* **42**, 959–962 (2017).
15. Wang, L. V. & Yao, J. A practical guide to photoacoustic tomography in the life sciences. *Nat. Methods* **13**, 627–638 (2016).
16. Ermolayev, V., Dean-Ben, X. L., Mandal, S., Ntziachristos, V. & Razansky, D. Simultaneous visualization of tumour oxygenation, neovascularization and contrast agent perfusion by real-time three-dimensional optoacoustic tomography. *Eur. Radiol.* **26**, 1843–1851 (2016).
17. Gottschalk, S., Fehm, T. F., Dean-Ben, X. L. & Razansky, D. Noninvasive real-time visualization of multiple cerebral hemodynamic parameters in whole mouse brains using five-dimensional optoacoustic tomography. *J. Cereb. Blood Flow Metab.* **35**, 531–535 (2015).
18. Knieling, F. et al. Multispectral optoacoustic tomography for assessment of Crohn's disease activity. *New Engl. J. Med.* **376**, 1292–1294 (2017).
19. Tzoumas, S. et al. Eigenspectra optoacoustic tomography achieves quantitative blood oxygenation imaging deep in tissues. *Nat. Commun.* **7**, 12121 (2016).
20. Yao, J. et al. High-speed label-free functional photoacoustic microscopy of mouse brain in action. *Nat. Methods* **12**, 407–410 (2015).
21. Schmued, L., Kyriakidis, K. & Heimer, L. In vivo anterograde and retrograde axonal transport of the fluorescent rhodamine-dextran-amine, Fluoro-Ruby, within the CNS. *Brain Res.* **526**, 127–134 (1990).
22. Bojak, I., Day, H. C. & Liley, D. T. Ketamine, propofol, and the EEG: a neural field analysis of HCN1-mediated interactions. *Front. Comput. Neurosci.* **7**, 22 (2013).
23. Dhir, A. Pentylenetetrazol (PTZ) kindling model of epilepsy.*Curr. Protoc. Neurosci.* **58**, 9.37.1–9.37.12 (2012).
24. Tang, J. et al. Noninvasive high-speed photoacoustic tomography of cerebral hemodynamics in awake-moving rats. *J. Cereb. Blood Flow Metab.* **35**, 1224–1232 (2015).
25. Durán-Riveroll, M. L. & Cembella, D. A. Guanidinium toxins and their interactions with voltage-gated sodium ion channels. *Mar. Drugs* **15**, 303 (2017).
26. Gottschalk, S. et al. Short and long-term phototoxicity in cells expressing genetic reporters under nanosecond laser exposure. *Biomaterials* **69**, 38–44 (2015).
27. Norup Nielsen, A. & Lauritzen, M. Coupling and uncoupling of activity-dependent increases of neuronal activity and blood flow in rat somatosensory cortex. *J. Physiol.* **533**, 773–785 (2001).
28. Kozberg, M. G., Ma, Y., Shaik, M. A., Kim, S. H. & Hillman, E. M. Rapid postnatal expansion of neural networks occurs in an environment of altered neurovascular and neurometabolic coupling. *J. Neurosci.* **36**, 6704–6717 (2016).
29. Vanni, M. P. & Murphy, T. H. Mesoscale transcranial spontaneous activity mapping in GCaMP3 transgenic mice reveals extensive reciprocal connections between areas of somatomotor cortex. *J. Neurosci.* **34**, 15931–15946 (2014).
30. Schroeter, A., Grandjean, J., Schlegel, F., Saab, B. J. & Rudin, M. Contributions of structural connectivity and cerebrovascular parameters to functional magnetic resonance imaging signals in mice at rest and during sensory paw stimulation. *J. Cereb. Blood Flow Metab.* **37**, 2368–2382 (2017).
31. Chen, T. W. et al. Ultrasensitive fluorescent proteins for imaging neuronal activity. *Nature* **499**, 295–300 (2013).
32. O'Herron, P. et al. Neural correlates of single-vessel haemodynamic responses in vivo. *Nature* **534**, 378–382 (2016).
33. Razi, A. & Friston, K. J. The connected brain: causality, models, and intrinsic dynamics. *IEEE Signal Process. Mag.* **33**, 14–35 (2016).
34. Lefebvre, J., Castonguay, A., Pouliot, P., Descoteaux, M. & Lesage, F. Whole mouse brain imaging using optical coherence tomography: reconstruction, normalization, segmentation, and comparison with diffusion MRI. *Neurophotonics* **4**, 041501 (2017).
35. Llinás, R. R., Leznik, E. & Urbano, F. J. Temporal binding via cortical coincidence detection of specific and nonspecific thalamocortical inputs: a voltage-dependent dye-imaging study in mouse brain slices. *Proc. Natl Acad. Sci. USA* **99**, 449–454 (2002).
36. Kneipp, M. et al. Effects of the murine skull in optoacoustic brain microscopy. *J. Biophotonics* **9**, 117–123 (2016).
37. Sieu, L. A. et al. EEG and functional ultrasound imaging in mobile rats. *Nat. Methods* **12**, 831–834 (2015).
38. Badura, A., Sun, X. R., Giovannucci, A., Lynch, L. A. & Wang, S. S. Fast calcium sensor proteins for monitoring neural activity. *Neurophotonics* **1**, 025008 (2014).
39. Dana, H. et al. High-performance GFP-based calcium indicators for imaging activity in neuronal populations and microcompartments. Preprint at https://www.biorxiv.org/content/10.1101/434589v1 (2018).
40. Akerboom, J. et al. Genetically encoded calcium indicators for multi-color neural activity imaging and combination with optogenetics. *Front. Mol. Neurosci.* **6**, 2 (2013).

41. Qian, Y. et al. A genetically encoded near-infrared fluorescent calcium ion indicator.*Nat. Methods* **16**, 171–174 (2019).
42. *American National Standard for Safe Use of Lasers* ANSI Z136.1 (Laser Institute of America, 2014).
43. Dean-Ben, X. L., Ozbek, A. & Razansky, D. Volumetric real-time tracking of peripheral human vasculature with GPU-accelerated three-dimensional optoacoustic tomography. *IEEE Trans. Med. Imaging* **32**, 2050–2055 (2013).
44. Wang, L. V. & Wu, H.-I. *Biomedical Optics: Principles and Imaging* (Wiley, 2007).
45. Abramowitz, M. & Stegun, I. A. *Handbook of Mathematical Functions: With Formulas, Graphs, and Mathematical Tables* Vol. 55 (Courer Corporation, 1964).
46. Zarchan, P. & Musoff, H. *Fundamentals of Kalman Filtering: A Practical Approach* (American Institute of Aeronautics and Astronautics, 2000).

Acknowledgements

The authors acknowledge grant support from the European Research Council (under grant agreement ERC-2015-CoG-682379) and the US National Institutes of Health (grants R21-EY026382 and UF1-NS107680). We also acknowledge the help of N. Tritsch and L. Mcley with reading and commenting on the manuscript.

Author contributions

S.G., O.D., B.M.L., M.A.H. and X.L.D.-B. performed the experiments. S.G., O.D., B.M.L., J.R., M.A.H. and X.L.D.-B. analysed and processed the data. S.G., X.L.D.-B., S.S. and D.R. validated the data analysis. S.G., S.S. and D.R. designed and supervised the study. All authors contributed to writing the manuscript.

Competing interests

The authors declare no competing interests.

Additional information

Supplementary information is available for this paper at https://doi.org/10.1038/s41551-019-0372-9.

Reprints and permissions information is available at www.nature.com/reprints.

Correspondence and requests for materials should be addressed to S.S. or D.R.

Publisher's note: Springer Nature remains neutral with regard to jurisdictional claims in published maps and institutional affiliations.

nature research

Corresponding author(s): Daniel Razansky

Last updated by author(s): Jan 26, 2019

Reporting Summary

Nature Research wishes to improve the reproducibility of the work that we publish. This form provides structure for consistency and transparency in reporting. For further information on Nature Research policies, see Authors & Referees and the Editorial Policy Checklist.

Statistics

For all statistical analyses, confirm that the following items are present in the figure legend, table legend, main text, or Methods section.

n/a	Confirmed	
☐	☒	The exact sample size (*n*) for each experimental group/condition, given as a discrete number and unit of measurement
☐	☒	A statement on whether measurements were taken from distinct samples or whether the same sample was measured repeatedly
☐	☒	The statistical test(s) used AND whether they are one- or two-sided *Only common tests should be described solely by name; describe more complex techniques in the Methods section.*
☐	☒	A description of all covariates tested
☐	☒	A description of any assumptions or corrections, such as tests of normality and adjustment for multiple comparisons
☐	☒	A full description of the statistical parameters including central tendency (e.g. means) or other basic estimates (e.g. regression coefficient) AND variation (e.g. standard deviation) or associated estimates of uncertainty (e.g. confidence intervals)
☒	☐	For null hypothesis testing, the test statistic (e.g. *F*, *t*, *r*) with confidence intervals, effect sizes, degrees of freedom and *P* value noted *Give P values as exact values whenever suitable.*
☒	☐	For Bayesian analysis, information on the choice of priors and Markov chain Monte Carlo settings
☒	☐	For hierarchical and complex designs, identification of the appropriate level for tests and full reporting of outcomes
☒	☐	Estimates of effect sizes (e.g. Cohen's *d*, Pearson's *r*), indicating how they were calculated

Our web collection on statistics for biologists contains articles on many of the points above.

Software and code

Policy information about availability of computer code

Data collection	Zen 2 microscope software (Carl Zeiss AG, Oberkochen, Germany) and Andor SOLIS software 4.21.30007.0 (Andor Technology Ltd., Belfast, UK).
Data analysis	All data analysis was performed in MatLab (MathWorks, Natick, United States).

For manuscripts utilizing custom algorithms or software that are central to the research but not yet described in published literature, software must be made available to editors/reviewers. We strongly encourage code deposition in a community repository (e.g. GitHub). See the Nature Research guidelines for submitting code & software for further information.

Data

Policy information about availability of data

All manuscripts must include a data availability statement. This statement should provide the following information, where applicable:

- Accession codes, unique identifiers, or web links for publicly available datasets
- A list of figures that have associated raw data
- A description of any restrictions on data availability

The authors declare that all data supporting the findings of this study are available within the paper and its Supplementary Information. All datasets generated for this study are available from the corresponding authors.

Field-specific reporting

Please select the one below that is the best fit for your research. If you are not sure, read the appropriate sections before making your selection.

☒ Life sciences ☐ Behavioural & social sciences ☐ Ecological, evolutionary & environmental sciences

For a reference copy of the document with all sections, see nature.com/documents/nr-reporting-summary-flat.pdf

Life sciences study design

All studies must disclose on these points even when the disclosure is negative.

Sample size	As the study is of exploratory nature, no pre-specified effect size and no sample-size calculation were needed.
Data exclusions	None.
Replication	Experiments were repeated in multiple animals.
Randomization	No randomization was required.
Blinding	No blinding was applied.

Reporting for specific materials, systems and methods

We require information from authors about some types of materials, experimental systems and methods used in many studies. Here, indicate whether each material, system or method listed is relevant to your study. If you are not sure if a list item applies to your research, read the appropriate section before selecting a response.

Materials & experimental systems

n/a	Involved in the study
☒	☐ Antibodies
☒	☐ Eukaryotic cell lines
☒	☐ Palaeontology
☐	☒ Animals and other organisms
☒	☐ Human research participants
☒	☐ Clinical data

Methods

n/a	Involved in the study
☒	☐ ChIP-seq
☒	☐ Flow cytometry
☒	☐ MRI-based neuroimaging

Animals and other organisms

Policy information about studies involving animals; ARRIVE guidelines recommended for reporting animal research

Laboratory animals	Eight- to twelve-week-old female C57BL/6J-Tg(Thy1-GCaMP6f)GP5.5Dkim/J and C57BL/6J-Tg(Thy1-GCaMP6s)GP4.12Dkim/J mice (The Jackson Laboratory, Bar Harbor, ME, USA; stock numbers 024276 and 025776, respectively) along with six-to twelve-week-old athymic female nude mice (Envigo, New Jersey, USA; stock number Foxn1nu 069) were used.
Wild animals	The study did not involve wild animals.
Field-collected samples	The study did not involve samples collected from the field.
Ethics oversight	In vivo experimentation was done in full compliance with the institutional guidelines of the Institute for Biological and Medical Imaging and with approval from the Government District of Upper Bavaria.

Note that full information on the approval of the study protocol must also be provided in the manuscript.